Dissertation

Imaging of Single Barium Atoms in Solid Xenon for Barium Tagging in the nEXO Neutrinoless Double Beta Decay Experiment

Submitted by

Timothy Walton

Department of Physics

In partial fulfillment of the requirements

For the Degree of Doctor of Philosophy

Colorado State University

Fort Collins, Colorado

Fall 2015

Doctoral Committee:

Advisor: William M. Fairbank, Jr.

Robert Wilson
Bruce Berger
Alan Van Orden

Copyright by Timothy Walton 2015

All Rights Reserved

Abstract

The nEXO experiment is designed to search for zero-neutrino double beta decay of the isotope ^{136}Xe, in order to better understand the nature of neutrinos. Since the daughter of this decay is barium (^{136}Ba), detecting the presence of ^{136}Ba at a decay site (called "barium tagging") provides an additional discriminator to reject backgrounds in the search for this decay. This would involve detecting a single barium ion from within a macroscopic volume of liquid xenon. One proposed barium tagging method is to trap the barium ion in solid xenon (SXe) at the end of a cold probe, and then detect the ion by its fluorescence in the solid xenon. William M. Fairbank Jr.'s group at Colorado State University has been working toward this goal with steady success for some time. In this thesis, I demonstrate successful detection of neutral Ba in SXe down to the single atom level, after deposition from vacuum.

Acknowledgements

Bill, Chris for all the help in the lab and building things, Shon and Brian for creating the system and training me (Shon) and for the preliminary results, Adam, Cesar, Kendy.

If you want the Leif thing, uncomment it in csuthesis.cls. It says something like ”this dissertation is typeset in ... designed by Leif Anderson.

Jamie and LEW, and other fam.

Table of Contents

CHAPTER 1

Introduction

Neutrinos have been at the forefront of discovery since their prediction by W. Pauli, who proposed in 1930 the existence of a neutral, unobserved particle to explain the apparent violation of energy conservation in beta decay [1]. He admitted that neutrinos (then deemed "neutrons" – what we now know as neutrons had not been discovered yet either) should be difficult to observe experimentally, but also that it seemed unlikely that they would never have been noticed before. As it turns out, they are much more difficult to observe than he predicted; they will not be noticed without extreme experimental techniques.

A theory formulated in 1933 by E. Fermi for beta decay [2], including the neutrino, would be the beginnings of weak theory, and the development of the very successful Standard Model (SM) of particle physics. However, the SM assumes that neutrinos are massless. The discovery of non-zero neutrino mass via neutrino oscillations in the late 1990s [3] shows that there is more new physics to be discovered – a path to follow in the further unification of physical theory.

Neutrinos are extremely difficult to study, but the rewards are profound. The favored See-saw Mechanism is a theory which predicts the extreme lightness of neutrinos, while also predicting very heavy neutrinos. The existence of heavy neutrinos in the high-energy environment of the early universe, coupled with the possibility of the violation of CP conservation which could slightly favor the production of matter vs. anti-matter in decays of these heavy neutrinos, could explain why the universe exists as we know it. [4]

If this theory is correct, then neutrinos would be described by the Majorana formulation rather than Dirac, and the process of neutrinoless double beta decay ($0\nu\beta\beta$) would be allowed. Observation of $0\nu\beta\beta$ would simultaneously demonstrate that neutrinos are Majorana particles, as well as give a measurement of the absolute mass itself [5]. This chapter outlines the current theory for neutrinos, and then describes the $0\nu\beta\beta$ experiments EXO-200 and nEXO, in order to motivate barium tagging for nEXO.

1.1. Neutrinos

Neutrinos are chargeless leptons which only interact via the weak force (and gravity). There are three known "flavors" of neutrinos, each corresponding to one of the three known leptons: ν_e, ν_μ, and ν_τ. These are the eigenstates in the basis of the weak force, so they are the states in which a neutrino will interact via the weak force.

1.1.1. Neutrino Oscillation and Mass.

The postulate that neutrinos have an energy basis which is different from the flavor basis predicts the phenomenon of oscillation – that the time evolution of an initially pure flavor state (as a neutrino will be produced) will result in a time-dependent probability of measuring the other two flavors as well.

The very small mass of a neutrino (assumed zero in the SM), specifically relative to its momentum, lets one write its Hamiltonian in terms of mass squared differences $\Delta m_{ij}^2 = m_i^2 - m_j^2$, where i,j = 1,2,3, referring to what we then call mass states. The mass basis is really the energy basis with the small mass approximation, along with dropping some constant terms in the Hamiltonian (which do not affect time evolution). Writing the time evolution in terms of mass squared differences means that neutrino oscillation experiments can produce measurements of these differences. In fact, the discovery of neutrino oscillation was the first (and only, so far) demonstration that neutrinos have a non-zero mass. Without neutrino mass (particularly without differences between the masses of the mass states), neutrinos would not oscillate.

Neutrino oscillation experiments also provide measurements on the amount of mixing between the flavor basis and the mass basis. We define the mixing between them by a rotation in terms of three mixing angles, θ_{12}, θ_{23}, and θ_{13}. Transformation between the flavor and mass bases is done with the following unitary matrix, called the Pontecorvo–Maki-Nakagawa-Sakata (PMNS) matrix:

$$\begin{aligned} U &= \begin{pmatrix} 1 & 0 & 0 \\ 0 & c_{23} & s_{23} \\ 0 & -s_{23} & c_{23} \end{pmatrix} \begin{pmatrix} c_{13} & 0 & s_{13}e^{-i\delta} \\ 0 & 1 & 0 \\ -s_{13}e^{i\delta} & 0 & c_{13} \end{pmatrix} \begin{pmatrix} c_{12} & s_{12} & 0 \\ -s_{12} & c_{12} & 0 \\ 0 & 0 & 1 \end{pmatrix} \begin{pmatrix} 1 & 0 & 0 \\ 0 & e^{i\alpha_1/2} & 0 \\ 0 & 0 & e^{i\alpha_2/2} \end{pmatrix} \\ &= \begin{pmatrix} c_{12}c_{13} & s_{12}c_{13} & s_{13}e^{-i\delta} \\ -s_{12}c_{23} - c_{12}s_{23}s_{13}e^{i\delta} & c_{12}c_{23} - s_{12}s_{23}s_{13}e^{i\delta} & s_{23}c_{13} \\ s_{12}s_{23} - c_{12}c_{23}s_{13}e^{i\delta} & -c_{12}s_{23} - s_{12}c_{23}s_{13}e^{i\delta} & c_{23}c_{13} \end{pmatrix} \begin{pmatrix} 1 & 0 & 0 \\ 0 & e^{i\alpha_1/2} & 0 \\ 0 & 0 & e^{i\alpha_2/2} \end{pmatrix} \end{aligned} \tag{1}$$

where $c_{ij} = \cos\theta_{ij}$ and $s_{ij} = \sin\theta_{ij}$. δ is a phase factor related to lepton CP violation, and α_i are Majorana phases.

Studying oscillations of neutrinos from different kinds of sources, with different energies and path lengths, can isolate sensitivities to the different parameters. For example, the study of solar neutrinos (neutrinos emanating from nuclear fusion reactions in the core of the sun) provides sensitivity to θ_{12} and Δm^2_{12}. The oscillation parameters so far measured shown in Table 1.1:

TABLE 1.1. Best-fit values for neutrino oscillation parameters, from a global fit to oscillation experiment data. Parameters which depend on the mass hierarchy have values for NH (IH). The atmospheric parameter Δm^2 is defined as $\Delta m^2 = \Delta m^2 = \Delta m^2_{31} - \Delta m^2_{21}/2 > 0 (\Delta m^2 = \Delta m^2_{32} + \Delta m^2_{21}/2 < 0)$. [6]

Parameter	Measurement ($\pm 1\sigma$)
Δm^2_{12}	$7.54^{+0.26}_{-0.22}$ 10^{-5} eV^2
$\lvert\Delta m^2\rvert$	2.43 ± 0.06 (2.38 ± 0.06) 10^{-3} eV^2
$\sin^2\theta_{12}$	0.308 ± 0.017
$\sin^2\theta_{23}$	$4.37^{+0.033}_{-0.023}$ ($4.55^{+0.039}_{-0.031}$)
$\sin^2\theta_{13}$	$0.0234^{+0.0020}_{-0.0019}$ ($0.0240^{+0.0019}_{-0.0022}$)
δ/π (2σ range)	$1.39^{+0.38}_{-0.27}$ ($1.31^{+0.29}_{-0.33}$)

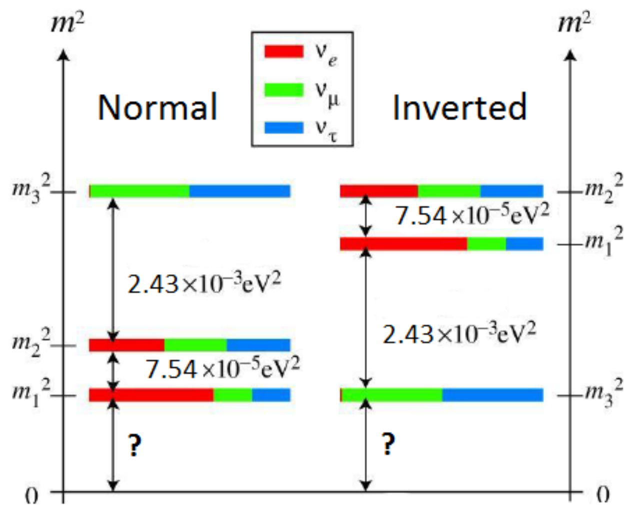

FIGURE 1.1. The two possible hierarchies of neutrino masses. The colors depict the mixing between the mass and flavor bases.

Note that only the absolute value of the atmospheric neutrino oscillation parameter Δm^2 is known. As a consequence, there are two possibilities for the hierarchy of the three neutrino masses. These are called the Normal and Inverted Hierarchies, as shown in Fig. 1.1. The correct mass hierarchy remains unknown, but next-generation neutrino experiments, possibly including nEXO, will be able to discern this.

Neutrino oscillation demonstrates that neutrinos have non-zero mass, and though oscillation experiments measure the mass squared differences, we still do not have a measurement of the absolute masses of the three neutrinos. Cosmology can put limits on the sum of the

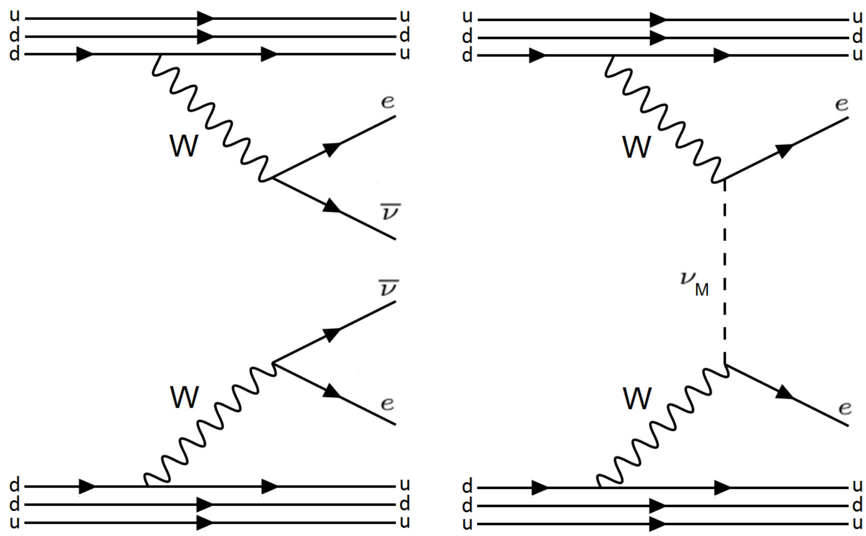

FIGURE 1.2. Two-neutrino (left) and neutrinoless (right) double beta decay.

three neutrino masses. The Planck collaboration reports an upper bound on this sum at $\sum_i m_i < 0.23$ eV [7]. The KATRIN experiment will search for absolute neutrino mass with limiting capability of $m_{\bar{\nu}_e} < 0.2$ eV (90% CL) by measuring the spectrum of tritium beta decay near the Q-value, searching for deviation from the spectrum with zero neutrino mass [8].

1.2. Double Beta Decay

Double beta decay is the simultaneous decay of two neutrons in a nucleus into two protons and two electrons. Two-neutrino double beta decay ($2\nu\beta\beta$), shown in Fig. 1.2(left), is allowed by the Standard Model and has been observed in eleven isotopes with half-lives between 10^{19} and 10^{21} years. Similar to beta decay, a neutrino accompanies each electron in this decay, broadening the spectrum of the summed electron energy. This is a second-order process, making it a rare decay, and requiring low backgrounds to measure.

$0\nu\beta\beta$, shown in Fig. 1.2(right), is a postulated mode of double beta decay. In this case, the neutrino is exchanged as a virtual particle (which would require that it is a Majorana particle), and there are no neutrinos in the final products. If discovered, not only would neutrinos be determined Majorana particles, but their absolute mass could also be measured as it relates to the $0\nu\beta\beta$ half-life according to Eqn. 2:

$$T_{1/2}^{0\nu} = (G^{0\nu}(Q,Z)|M^{0\nu}|^2 \langle m_\nu \rangle^2)^{-1} \tag{2}$$

where $T_{1/2}^{0\nu}$ is the $0\nu\beta\beta$ half-life, $G^{0\nu}$ is a known phase space factor, and $M^{0\nu}$ is a model-dependent nuclear matrix element. The effective electron neutrino mass $\langle m_\nu \rangle$ is the expectation value of the mass for a pure electron neutrino:

$$\langle m_\nu \rangle = \sum_i U_{ei}^2 m_i. \tag{3}$$

The sum of the energies of the emitted electrons in double beta decay will serve as the distinction between the two-neutrino and zero-neutrino modes, shown in Fig. 1.3. In the two-neutrino mode, the total decay energy is shared probabilistically between the electrons and the neutrinos (the nucleus recoil energy is negligible), resulting in a broad distribution in the summed electron energy. (Recall the similarly broad electron energy in single beta decay, which ultimately led to discovery of the neutrino involved.) But in the zero-neutrino mode, all of the decay energy is carried away by the two electrons, resulting in only a single allowed value for the summed electron energy – a peak in the summed electron energy spectrum at the Q-value.

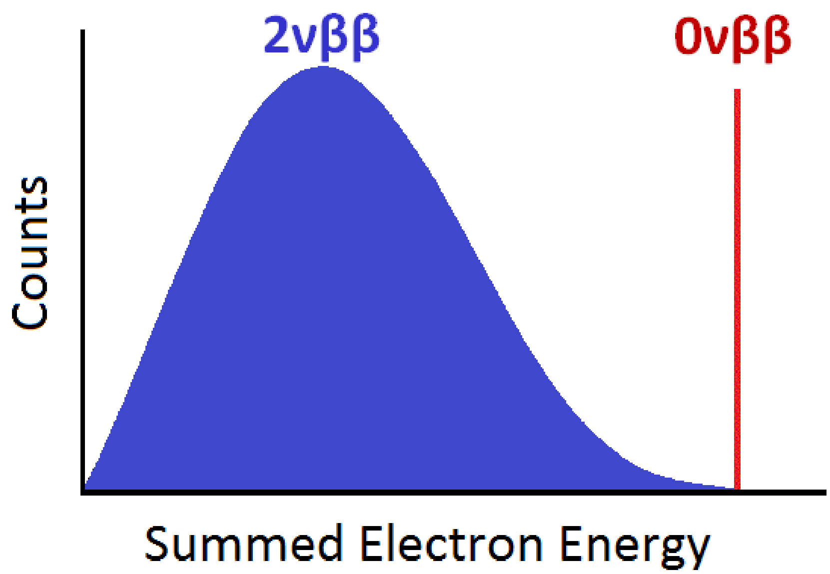

Figure 1.3. Conceptual two-neutrino (blue) and zero-neutrino (red) double beta decay spectra.

The rarity of double beta decay requires very low backgrounds, especially around the Q-value for the $0\nu\beta\beta$ search. The next sections describe the experiments EXO-200 and its next-generation successor, nEXO.

1.3. Enriched Xenon Observatory

EXO-200 and nEXO (EXO standing for Enriched Xenon Observatory) are a progression of two experiments, each a LXe time projection chamber (TPC) designed to study the double beta decay of the isotope ^{136}Xe, and ultimately to search for the zero-neutrino mode. Xe is fairly unique among the double beta decay isotopes in that it can be studied in a gas or liquid TPC instead of solid crystals or foils. The 3D event position reconstruction abilities of a TPC have advantages in background reduction, described in section 1.3.1. Purification of Xe is straightforward and can be done continuously in a detector. LXe is transparent, and produces substantial ionization and scintillation at 178 nm when energy is deposited in the LXe [9]. A liquid TPC approach also offers the opportunity to identify, or "tag", the daughter Ba^{++} at the site of the double beta decay event, which would provide a background-free identification of $0\nu\beta\beta$ [10]. Barium tagging is the focus of our group at CSU and is the subject of this thesis. The following sections decribe the EXO-200 experiment, as well as nEXO, the next-generation tonne-scale LXe TPC which is now in the design stages. EXO-200 does not have barium tagging implemented, but it is hoped that nEXO will.

1.3.1. EXO-200. EXO-200 has been operational since 2011. It is a TPC using 110 kg of active LXe enriched to 80.672% ± 0.14% ^{136}Xe [9], designed to probe Majorana neutrino masses down to around 109-135 meV (the range covers different matrix element calculations) [11], and is located about half a mile underground in the Waste Isolation Pilot Plant (WIPP) near Carlsbad, NM. This mine is in a salt basin, which contains lower levels of Uranium and Thorium than a more typical mine in rock.

A schematic of the TPC in the class 100 cleanroom is shown in Fig. 1.4. Several layers of lead wall surround the copper cryostat, which is filled with HFE-7000, a cryogenic fluid which keeps the TPC cooled to LXe temperatures, as well as aids in shielding. The TPC vessel is made of low-radioactivity copper, and is kept as thin as possible to minimize backgrounds. Scintillating panels on the outside of the cleanroom provide muon veto.

A cut-away view of the EXO-200 detector is shown in Fig. 1.5. It is two mirrored TPCs which share a cathode. The detection planes are a combination of ionized charge induction/collection wires and large area avalanche photodiodes (LAAPDs) which detect scintillation light [12].

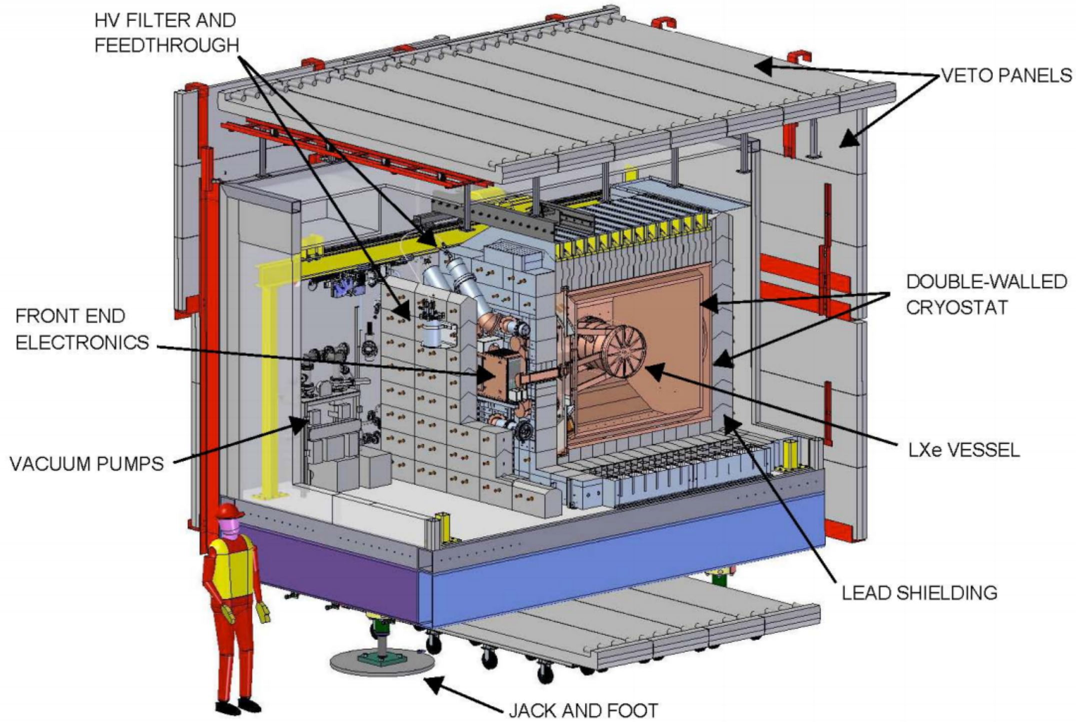

FIGURE 1.4. Drawing of cleanroom laboratory in the WIPP drift.

A photograph of the detection plane is shown in Fig. 1.6, and a schematic of event detection is shown in Fig. 1.7. When a double beta decay event occurs in the LXe, the energetic electrons ionize many surrounding Xe atoms, as well as produce a scintillation signal. Scintillation light provides a time stamp for the event as well as an energy measurement.

The cathode is set to -8 kV, providing an electric field of 374 V/cm across the 20 cm drift length of each TPC. Ionized electrons drift from the decay site, first passing the v-wires, which receive an induction signal, and are then collected by the u-wires, which are set at a 60° angle from the v-wires. An electric field of 778 V/cm between the u- and v-wires ensures 100% v-wire transparency. The charge collection provides an energy measurement complimentary to that of the scintillation. Together, the u- and v-wires give an x/y position measurement for the event. The time between the initial scintillation detection and the charge collection give a

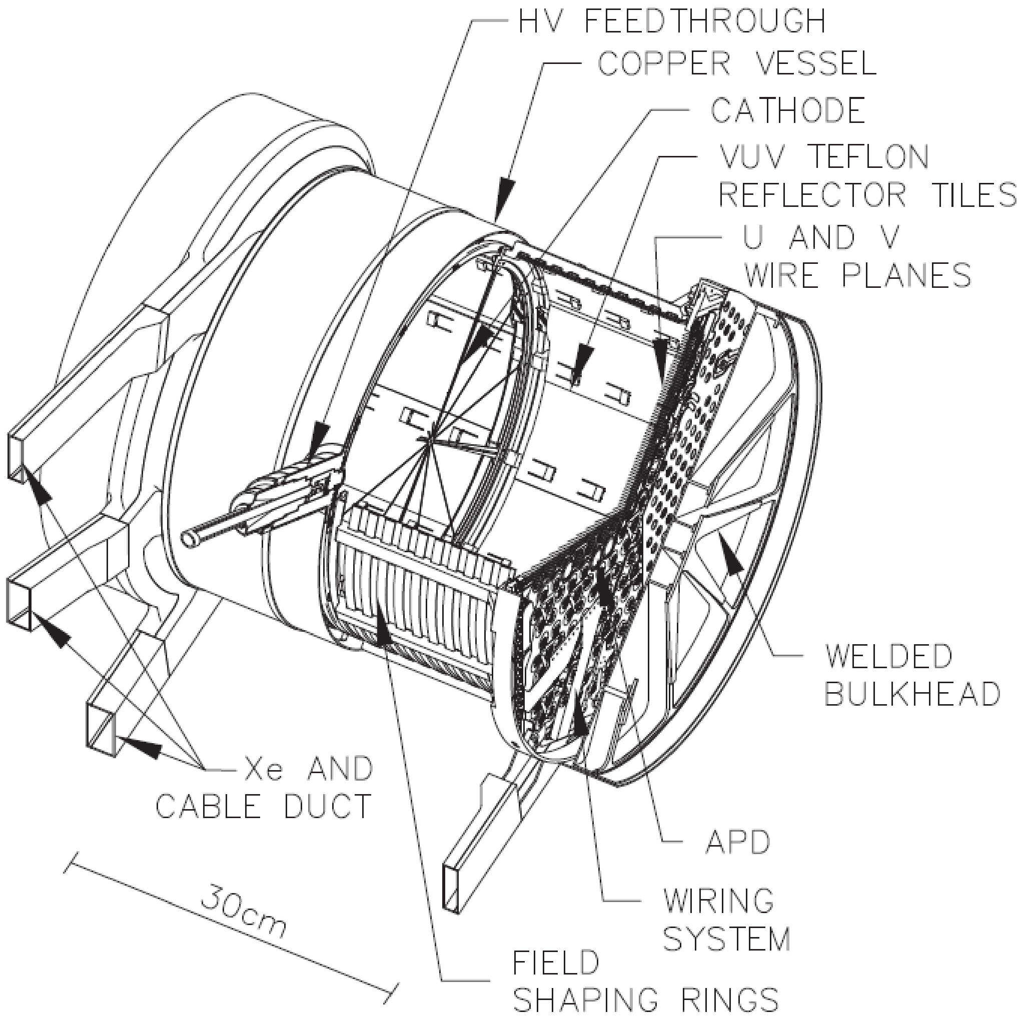

Figure 1.5. EXO-200 TPC cutaway [9].

z position, and a 3D position can be reconstructed for the event. [9] Additional scintillation resulting from recombination of ionized electrons leads to a well-known microscopic anti-correlation between ionization and scintillation signals [13]. Applying this to the combination of those signals improves the energy resolution. This correction defines a combined energy axis, called the rotated energy. Energy resolution is important in a $0\nu\beta\beta$ search, as it distinguishes those events from $2\nu\beta\beta$ events in the tail of their spectrum.

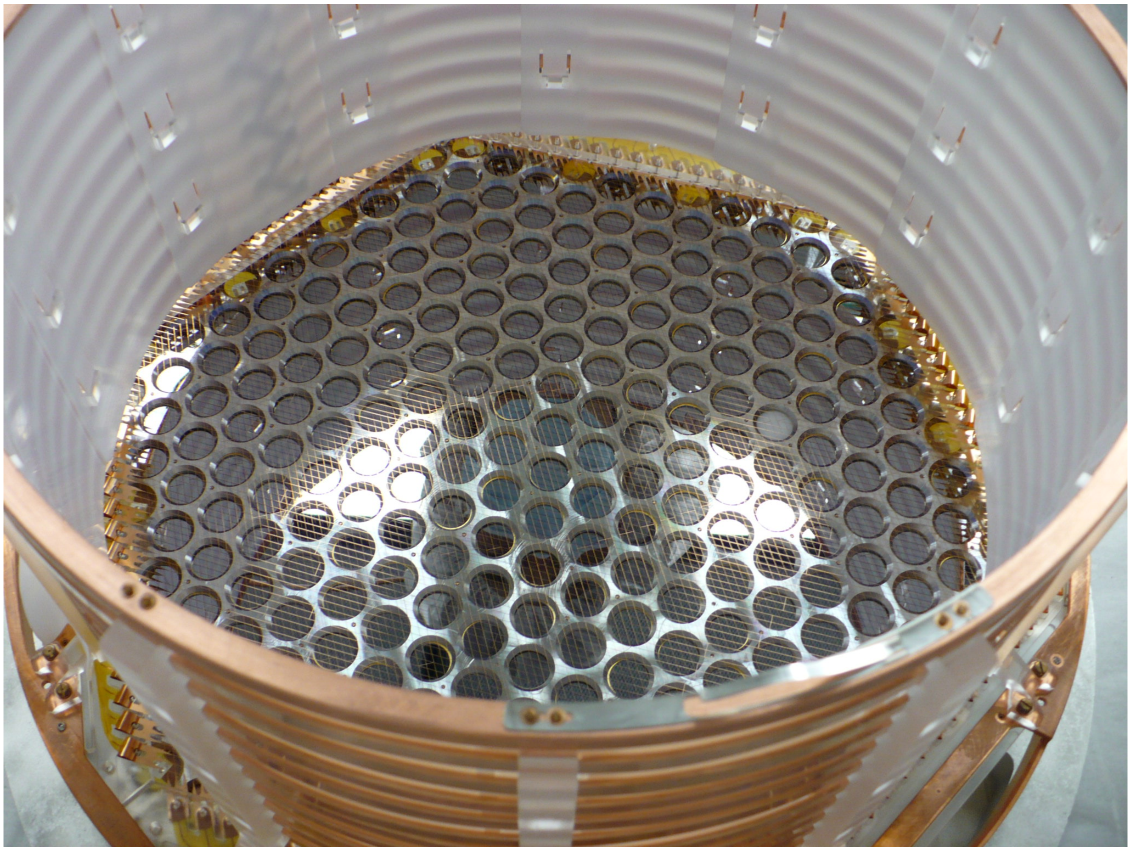

FIGURE 1.6. View of the detection plane in one of the two EXO-200 TPCs.

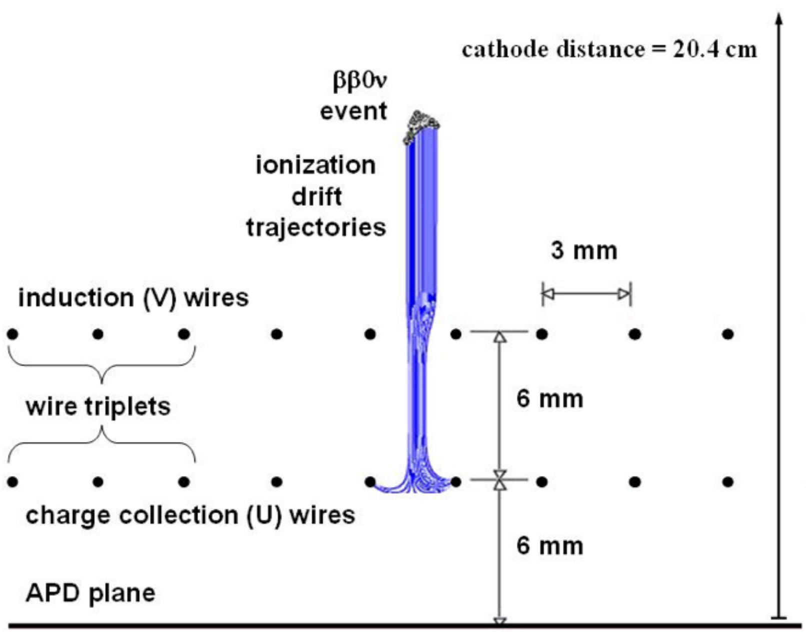

FIGURE 1.7. EXO-200 event detection.

Having a reconstructed 3D event position is important in several ways. Firstly, position-based corrections on scintillation and charge collection can be applied. For charge, electronegative impurities in the LXe will absorb the drifting charge, requiring a drift-length (z-position) correction. High purity levels, measured in terms of electron lifetime, of 2-3×10^3 μs are maintained in EXO-200, resulting in a small correction of few % for maximal drift lengths. For scintillation, a 3D correction is applied, as some regions have more efficient light collection by the LAAPDs. A 3D position also allows a fiducial volume to be defined. The effect of radio-impurities on detector surfaces, e.g. radon daughters collecting on the cathode, is mitigated by defining a stand-off distance required for events used in analysis. Finally, 3D reconstruction allows the distinction between single-site (SS) and multi-site (MS) events. A MS event is one where two spatially separated events occur in the same 2048-μs time window. These are mostly caused by gamma rays interacting in the LXe, which can Compton-scatter several times. Rejecting MS events strongly separates gamma events from double beta decay events. [9] Of course, barium tagging will also require a 3D reconstructed position in nEXO.

The final data set is fit using a combination of probability distribution functions (PDFs) for $0\nu\beta\beta$, $2\nu\beta\beta$, and all possible backgrounds. Fits to the final energy spectrum data for (a) SS events, and (b) MS events are shown in Fig. 1.8 for the most recent $0\nu\beta\beta$ search analysis. The green bands beneath each plot show the residuals vs. energy. The $2\nu\beta\beta$ spectrum, in gray, dominates the backgrounds in the SS spectrum. The vertical red lines in the SS spectrum outline the $\pm 2\sigma$ region of interest around the Q-value, where the $0\nu\beta\beta$ peak will lie. The insets are a zoom into this region. The fit value for $0\nu\beta\beta$ in this dataset is non-zero, but it is consistent with the null hypothesis at 1.2σ. This sets an upper limit on the

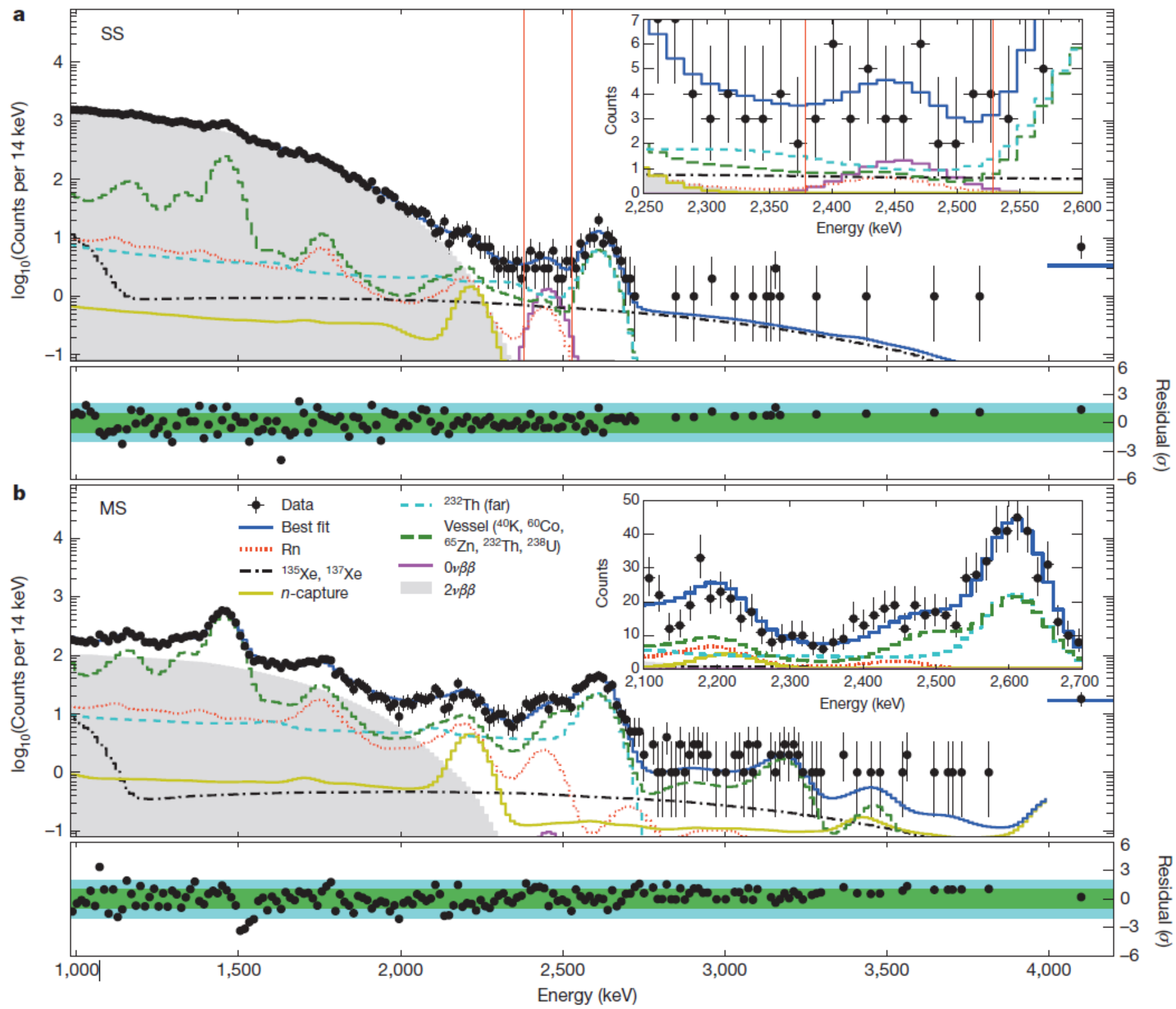

FIGURE 1.8. EXO-200 energy spectrum from $0\nu\beta\beta$ search analysis [14].

$0\nu\beta\beta$ half-life at $T_{1/2}^{0\nu\beta\beta} < 1.1 \times 10^{25}$ yr (90% CL), which corresponds to $\langle m_{\nu_e} \rangle$ <190-450 meV depending on nuclear matrix element calculations [14]. EXO-200 reports the $2\nu\beta\beta$ half-life measurement in [9] of $T_{1/2}^{2\nu\beta\beta} = 2.165 \pm 0.016(\text{stat}) \pm 0.059(\text{sys}) \times 10^{21}$ yr. This is consistent with previous measurements by EXO-200 in 2011 [15] and KamLAND-ZEN in 2012 [16].

1.3.2. nEXO. The next-generation successor to EXO-200 is nEXO, a tonne-scale LXe TPC which will probe Majorana neutrino masses down to the 10 meV scale. The sensitivity projections for nEXO are shown in Fig. 1.9, along with those of EXO-200. nEXO will reach phase space where the two possible mass hierarchies begin to split; if nEXO successfully

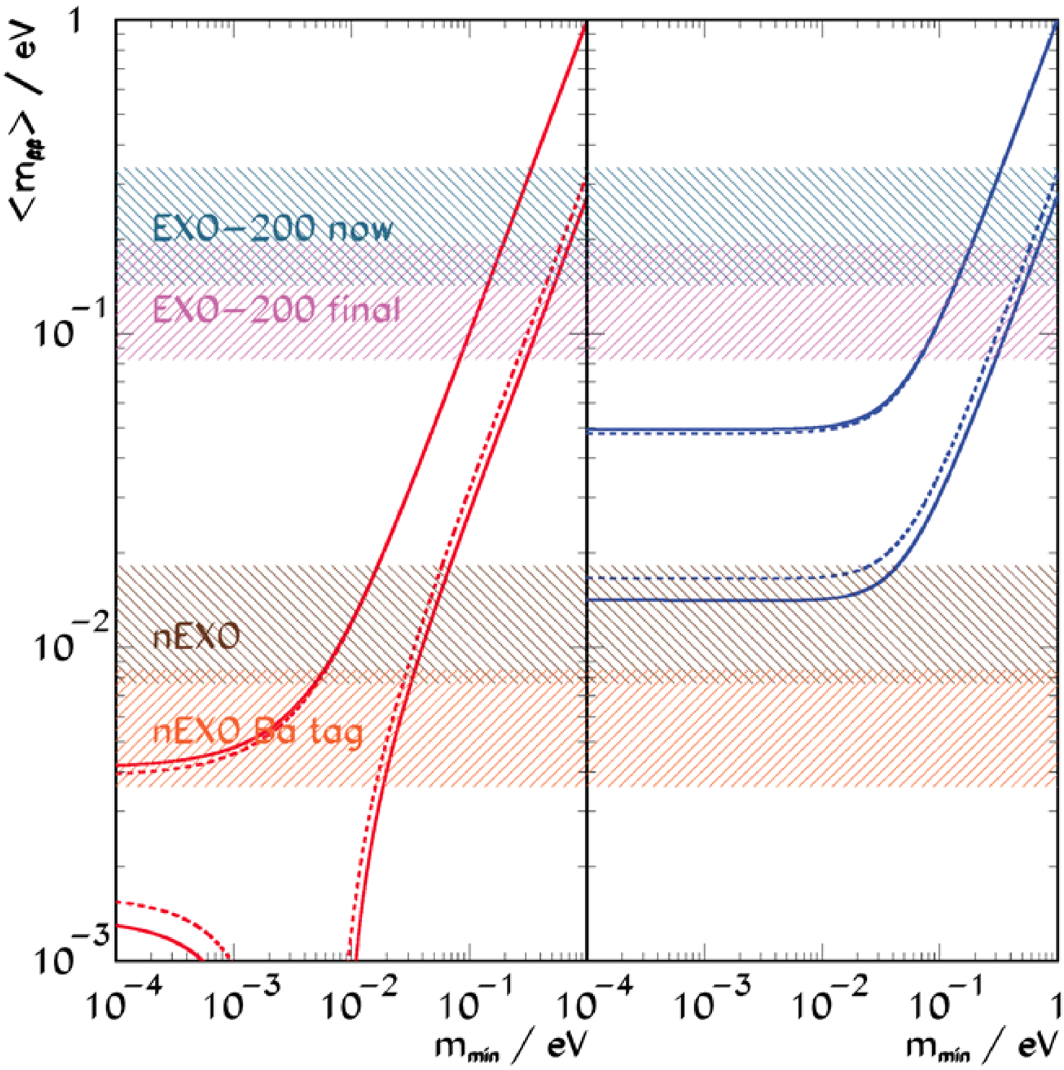

FIGURE 1.9. nEXO projected sensitivity to the Majorana neutrino mass vs. the minimum of the three masses m_{min}. check for updated version

observes $0\nu\beta\beta$ in these regions, it may be able to also determine the mass hierarchy. Barium tagging will push the sensitivity further into the region allowed only by the normal hierarchy [ref for this?].

A schematic of the experimental setup is shown in Fig. 1.10 in one of the possible locations for nEXO, the SNOLAB cryopit. Similar to EXO-200, the copper-housed TPC will be submerged in HFE fluid, inside a copper cryostat. The cryostat will be insulated and submerged in a large volume of water shielding, in which photo-multiplier tubes could

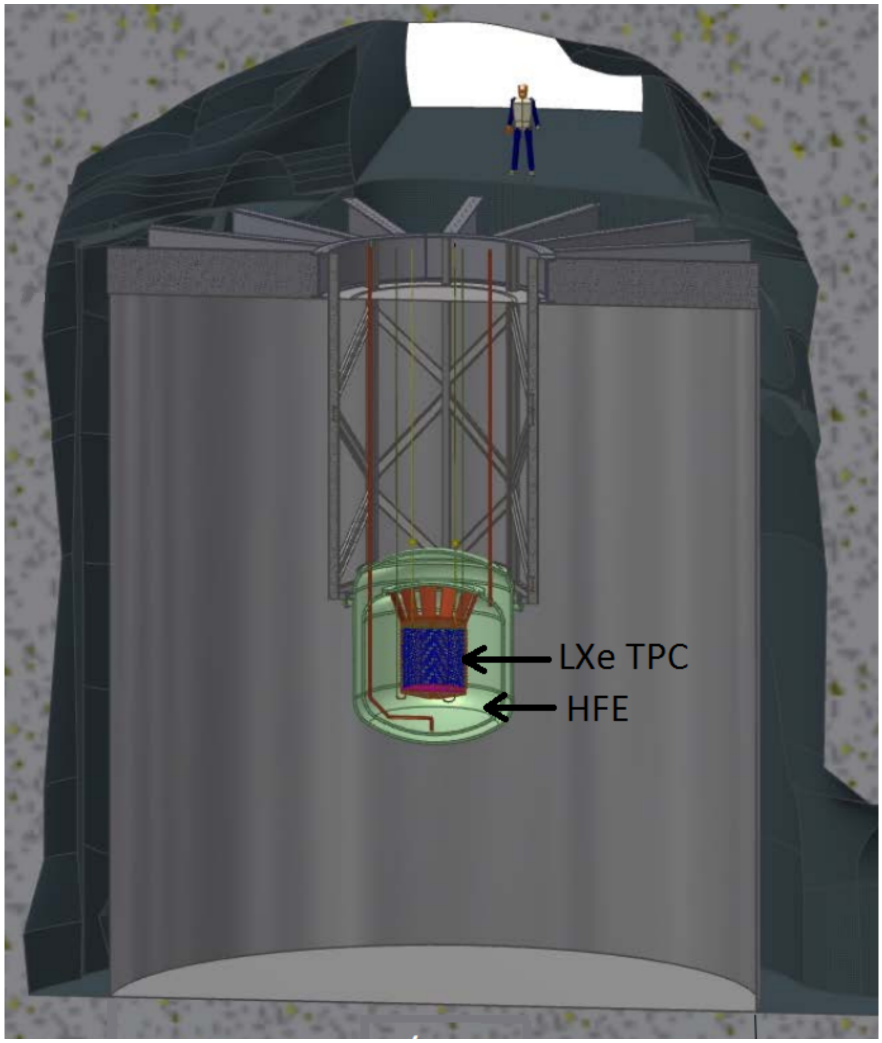

FIGURE 1.10. nEXO TPC in the SNOLAB cryopit.

provide muon veto by observing Cherenkov radiation. nEXO will be a single TPC with charge and light readouts at opposing ends of the TPC. Rather than wires, nEXO will use tile electrodes for charge readout, shown in Fig. 1.11.

1.3.3. BARIUM TAGGING. The backgrounds observed around the Q-value in EXO-200 can be expected to scale up with the size of nEXO. But with the veto power of barium tagging, nEXO's sensitivity to $0\nu\beta\beta$ scales with the total ^{136}Xe mass in the detector, vs. the square root of that mass without barium tagging.

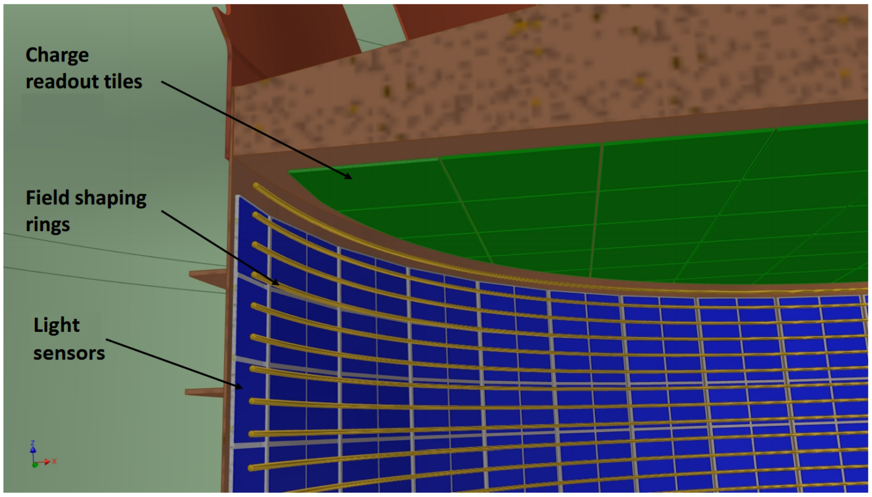

FIGURE 1.11. nEXO readout.

Several possible barium tagging techniques have been proposed. Perhaps the most natural concept is to direct one or more lasers at the decay site to induce fluorescence of the barium daughter. This technique was explored thoroughly by Fairbank's group, and was abandoned when reliable fluorescence of Ba^+ in LXe could not be observed [ref Kendy's thesis, after kamland in list].

Three barium tagging techniques continue to be explored. One of these is to grab the daughter on a surface, brought to the decay site by a probe, and then move it to a location where it can be desorbed from that surface by an infrared laser, and subsequently resonantly ionized by two lasers in order to detect it by time-of-flight spectroscopy. The apparatus for the study of this method is described in [17], along with some initial results. Another concept is to also grab the daughter on the surface of a probe, but then to thermally desorb it for subsequent trapping and detection [ref upcoming Liang paper, after Twelker].

The other remaining technique for barium tagging, now the concentration of Fairbank's group and the subject of this thesis, is called tagging in SXe. Here, a cold probe would go to the site of the candidate $0\nu\beta\beta$ event in order to trap the Ba/Ba^+ in a small amount of SXe, and then observe it by its laser-induced fluorescence in the SXe, a technique called matrix isolation spectroscopy.

A concept for a probe is shown in Fig. [ref fig cryoprobe]. The SXe forms on a sapphire window or plug. Sapphire is a good candidate for a substrate; it has good thermal conductivity at low temperature, and is extremely transparent. An excitation laser would be brought into the probe through a fiber, and aimed through the sapphire to excite the Ba/Ba^+ in the SXe. A return fiber could collect the laser reflections to measure the SXe thickness via interference fringes. The Ba/Ba^+ fluorescence would then be collected by a lens/filter system and imaged onto a CCD. Additional components, not shown, would be required for cooling the sapphire, either by liquid He or by a Joule-Thompson nozzle, as well as a thermometer.

Whether the daughter Ba will neutralize or remain ionized is not yet known. It is however expected that a Ba^{++} ion will neutralize once to Ba^+ in lXe, since the lXe conduction band gap is slightly less than the ionization potential for Ba^+ [10]. Further neutralization could also occur. A study of neutralization of alpha decay daughters in EXO-200 has observed a fairly equal balance of neutralized daughters vs. ionized daughters [ref alphaion]. The feasibility of detecting single Ba ions as well as atoms is still of interest.

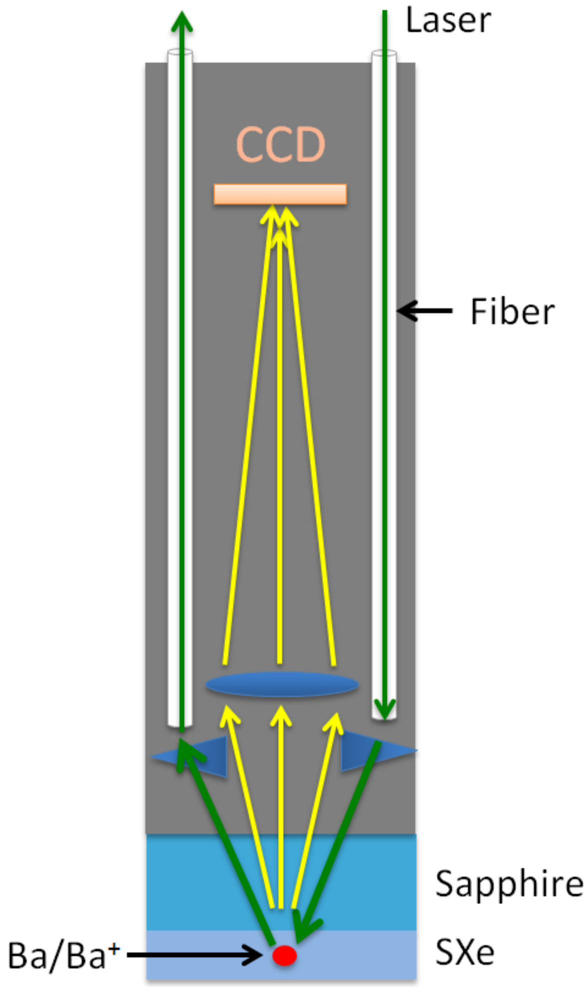

FIGURE 1.12. Concept for a cryoprobe containing excitation/collection optics.

CHAPTER 2

Theory

2.1. Ba/Ba$^+$ Spectroscopy in Vacuum

The lowest-lying energy levels in vacuum for Ba and Ba$^+$ are shown in Fig. 2.1. For Ba, the main transition is between the ground $6s^2\ {}^1\mathrm{S}_0$ to the excited $6s6p\ {}^1\mathrm{P}_1$ state. Spin(?)-suppressed transitions between the P state and three metastable D states results in a decay in to a D state after about 350 excitations. For Ba$^+$, two strong transitions exist between the ground $6s\ {}^2\mathrm{S}_{1/2}$ and the $6p\ {}^2\mathrm{P}_{1/2}$ and $6p\ {}^2\mathrm{P}_{3/2}$ excited states. Transitions to the two metastable D states are higher than for the atom, resulting in a decay into a D state after about 4 excitations.

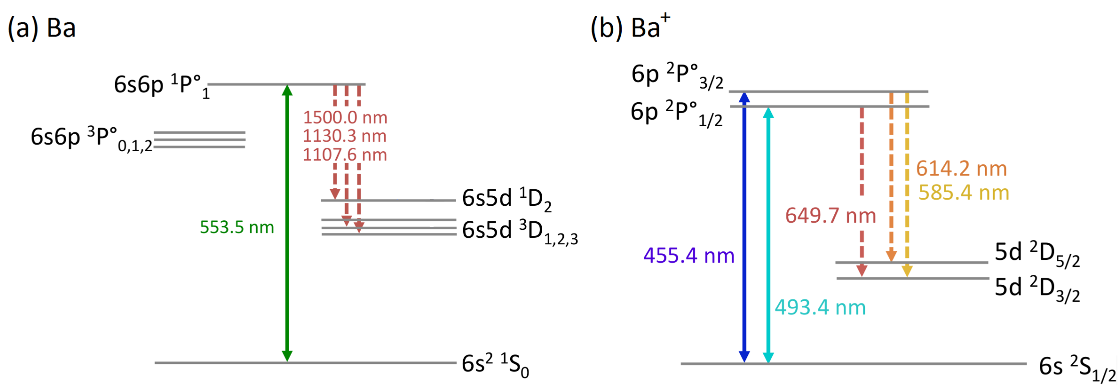

Figure 2.1. Energy level diagrams for (a) Ba and (b) Ba$^+$

These energy levels and their transition rates are well known, and are documented in the NIST tables [ref]. Single atom/ion detection by spectroscopy generally requires lasers to provide transitions out of the metastable D states once the atom/ion decays into one of them, in addition to the main excitation laser. For the atom, this requires three additional infrared lasers, and single atom trapping/detection in a magneto-optical trap (MOT) is achieved in [ref Ba MOT]. Single Ba$^+$ observation requires only two lasers if the ${}^2\mathrm{P}_{1/2}$ excited state is used. This is demonstrated in [ref something that does this ... is there something? How about the Carleton group? I think MOE has a reference to it maybe – yeah, its [19]].

2.1.1. 5- OR 6-LEVEL MODEL? This could be for just the vacuum, and the in-matrix could reference it with changes (so I guess this would just be 5-level).

2.2. Matrix Isolation Spectroscopy

May be good matrix isolation theory references in Ba Spec.

The spectroscopy of a species trapped in an inert solid matrix is called matrix isolation spectroscopy, the concept of which was pioneered around 19?? by [that one guy] [ref ... maybe [1] of ba spec]. Though absorption and emission are significantly broadened and shifted, a species can retain properties of its vacuum counterpart, such as quantum numbers.

Studies of some matrix isolation systems have been made. The most thoroughly studied has been Na(?) in solid matrices of (Ar, Kr, Xe ?)... (Na? Mg?)...[refs]

We are of course interested in the spectroscopy of Ba and/or Ba^+ in SXe matrices, and this particular system has not been studied until recently. The first report of the spectroscopy of neutral Ba in SXe, along with candidate fluorescence peaks for Ba^+ in SXe, was published by our group in [ref ba spec], and conversations following this publication with ???'s group in ??? have confirmed our basic observations of the absorption spectrum of Ba in SXe.

From here forward I will refer to the host species as Xe and the guest as Ba/Ba^+, specific to our system. The leading interaction between [put this here if the van der waals is only necessarily the force for Ba in particular] the Ba/Ba^+ and a neighboring Xe atom is a (the) Van Der Waals (sp?) force, an induced dipole-dipole interaction. Xe is the most polarizable (sp?) of the noble gases.

The forms for this force(?) is shown in Eqn. [ref van der ba] for Ba and Eqn. [ref van der ba+] for Ba^+. Talk about it.

This binding between the Ba/Ba^+ and its surrounding Xe atoms results in vibrational modes, and the Franck Condon (sp?) principle applies. Fig. [ref fig franckcondon] helps illustrate this effect. In a cold matrix, the system will be in the ground vibrational state before excitation. The distribution of the wavefunction, even for the ground state alone, overlaps in space in general with more than one of the excited state vibrational modes, resulting in a broadening in energy of the absorption.

Rapid decay occurs to the lowest vibrational mode in the excited state before electronic decay can occur [ref] [is this just for Ba?]. Then a similar broadening in emission energy occurs as several overlapping vibrational mode wavefunctions exist in the ground electronic state, and a redshift is also observed as some energy was dissipated into phonons in the crystal in vibrational mode decays. **(How can you get a blueshift?)**

Shifts and broadening in absorption and emission depend in general on the distribution of Xe atoms around the Ba/Ba^+. The fcc crystal structure of the Xe restricts these environments to discrete number of so-called matrix sites, defined by (a) whether the Ba/Ba^+ is [intersituational or whatever – is that still a thing?], and (b) the number of vacancies in the Xe matrix surrounding the Ba/Ba^+. Experimental observation of emission peaks from different matrix sites of [Na] in solid noble gases is reported in [ref(s)], with theoretical calculations in [ref(s)] attributing observed peaks to specific vacancy distributions defining the matrix sites (maybe this has been done?).

Energy level transition probabilities can also be affected in a matrix. Distortions in electron wavefunction shapes by asymmetric matrix sites can affect radiative transitions by altering parity [ref]. If electronic potential energy curves cross each other, nonradiative transitions can also become allowed for otherwise forbidden transitions [ref]. (Is a phonon emission called a nonradiative transition / does this actually happen?)

Jahn-Teller?

The detectability of a single atom/ion can depend greatly on altered transition rates. For example, in the Ba atom, matrix-allowed decay of the $^1P_1$ to the ^3P states could be much stronger than the main transition back to ground, which would suppress fluorescence and make single-atom detection impossible. But the matrix could also help by strengthening decays from the D states back to ground, eliminating any need for re-pump lasers to keep the transition cycle going.

CHAPTER 3

Experimental

This chapter describes the apparatus at Colorado State University which has been used for all described studies of Ba/Ba^+ fluorescence in SXe after deposition in vacuum. Our main barium source, a Ba^+ ion beam, is first described, as well as a purely Ba neutral source. The co-deposit of Ba/Ba^+ with Xe gas onto a cold sapphire window, subsequent laser excitation, and finally the collection optics for the fluorescence are described.

3.1. Ion Beam

The full ion beam is shown in Fig. 3.1. This is a clean source of Ba^+ which can do a very wide range of deposit sizes, from billions of ions in a focused laser region all the way down to the single-ion level , and even deposit sparsely enough to scan a focused laser over spatially separated ions.

3.1.1. Ion Source.

Ba^+ ions are produced in a Colutron ion gun system [20]. The source is shown in Fig. 3.2. A solid barium charge is placed into the hollowed end of a stainless steel rod, which is then inserted into the discharge chamber, near the hot filament. The barium vaporizes, and escapes the hollowed rod around a loosely threaded set screw. The source is designed to produce a discharge between the anode plate and the filament cathode, through an argon buffer gas leaked into the source chamber. This controlled discharge would then also ionize atoms from the solid charge to produce the desired ion beam, and Ar ions would be filtered out. However, to avoid contamination of the SXe matrix with residual Ar gas, the buffer gas is not used in this work. We are still able to maintain a discharge between the filament and anode circuits. The longevity of ion current from a single charge

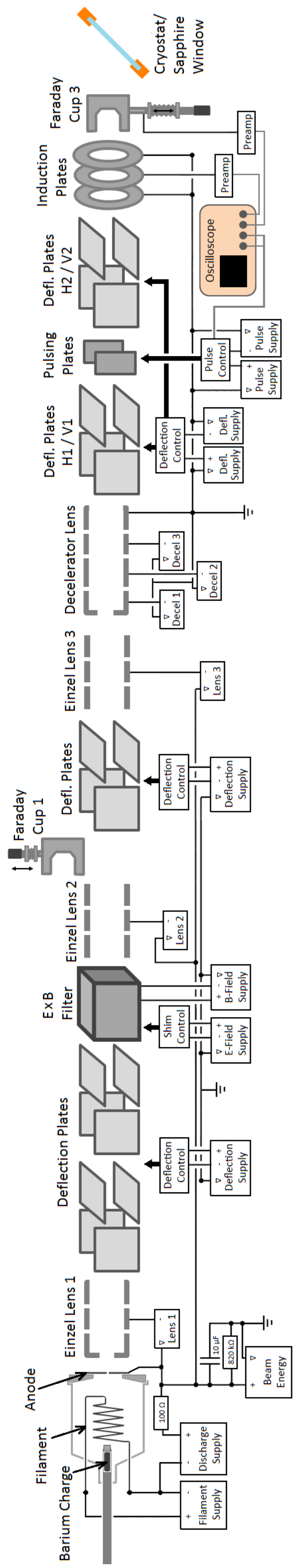

FIGURE 3.1. Ba$^+$ ion beam.

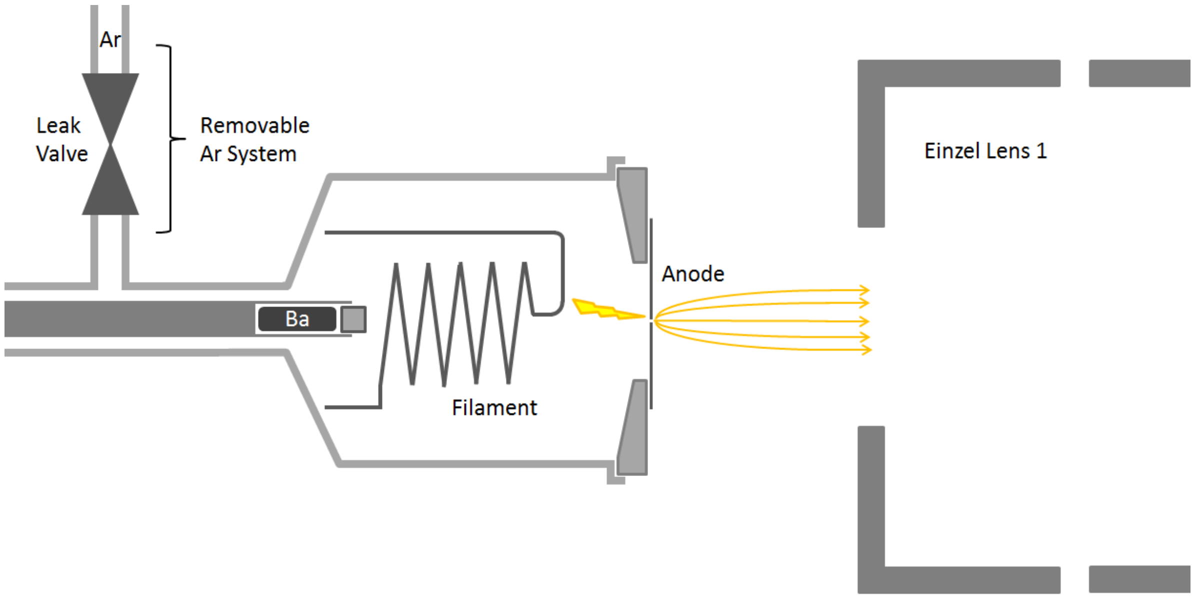

FIGURE 3.2. Ba^+/Ar^+ ion source.

(at least several 10s of hours) suggests that Ba is coating the inner walls of the chamber and is depleted slowly. This is supported by the observation of white oxidation of the inner source parts after a few minutes of exposure to air when opening the system. The discharge produces a plasma, containing barium ions, which escapes the chamber through a small hole in the anode, where it enters the acceleration region. The acceleration potential is 2 kV, between the ion source anode and an aperture, which is the first element of Einzel lens 1. This lens approximately collimates the ion beam for passage through the E×B velocity filter.

3.1.2. E×B VELOCITY FILTER. The E×B velocity filter selects Ba^+ by creating perpendicular electric and magnetic fields, which produce opposing forces on charged particles moving straight through the filter. The opposing forces will be equal for ions with velocity $v = \frac{E}{B}$. Since ion velocity is determined by mass (m), charge (q) and beam potential (V), the filter selects ions satisfying Eq. 4:

$$\frac{m}{q} = \frac{2VB^2}{E^2} \tag{4}$$

where B and E are the magnetic and electric fields, respectively. Those fields are chosen such that the forces are equal for Ba^+. Other ions will be deflected.

The E×B filter is shown in Fig. 3.3. Electromagnets provide the vertical magnetic field. Electrode plates and field-shaping guard rings provide the horizontal electric field. The guard rings prevent a lensing and astigmatism effect from fringe fields of the plates [20].

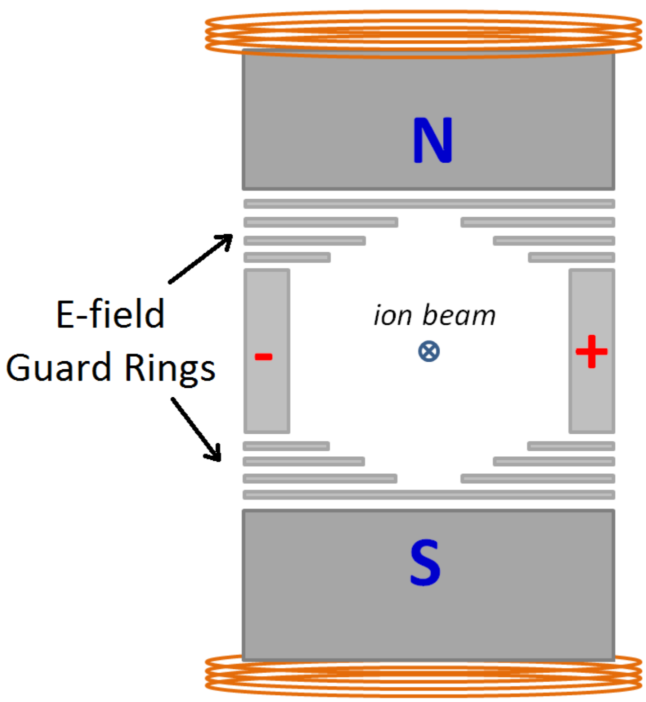

FIGURE 3.3. Colutron E×B ion velocity filter.

3.1.3. OTHER BEAM COMPONENTS. The first three sets of deflection plates can be used for beam diagnostics, and are set to 0 V during normal operation. The deflection plates just before the pulsing plates, H1 and V1, are set to constant values of 50 V and 0 V, respectively, which have been selected such that the beam, in both pulsing and continuous modes, can be deposited at the sapphire window for reasonable settings on the final deflection plates, H2 and V2. As described in 3.1.5, different settings in H2/V2 are required for peak ion current in Faraday cup 3 vs. peak deposit at the window.

Einzel lens 2 focuses the beam the pass through the aperture in the first element of the decelerator lens. Einzel lens 3 is not used in this setup. The decelerator lens can be used to vary Ba^+ deposit energy, but it in this work it acts as an Einzel lens with only the second element at voltage, and it focuses the beam at Faraday cup 3 (there is no Faraday cup 2 in this setup). Faraday cup 3 measures the ion current during experiments, and is retracted when deposits are being made. Its use in deposit calibration is described in 3.1.5. Faraday cup 1 is used for beam diagnostics, and is usually retracted on its bellows.

3.1.4. Ion Beam Pulsing. When running in pulsing mode, the pulsing plates are first set to 200 V and -200 V to deflect the beam, and are pulsed to 0 V for 1 μs for each pulse. The pulsing circuit is shown in Fig. 3.4. Square waves, triggered by LabVIEW at 500 Hz, enter the circuit at (a). The transformed pulse triggers the MOSFET switch, which closes the circuit for the period of the pulse.

The induction plates observe pulses during a deposit. Pulses just prior to a deposit can be observed by cup 3 (as well as the induction plates) for a local measurement of ion current in the pulses. eV Products pre-amplifiers convert the ion current to voltage signals which are read out with a digital oscilloscope. An example of an oscilloscope readout of 16 averaged pulses is shown in Fig. 3.5(left). The pre-amp circuit is solved to retrieve the original current, given by Eqn. 5:

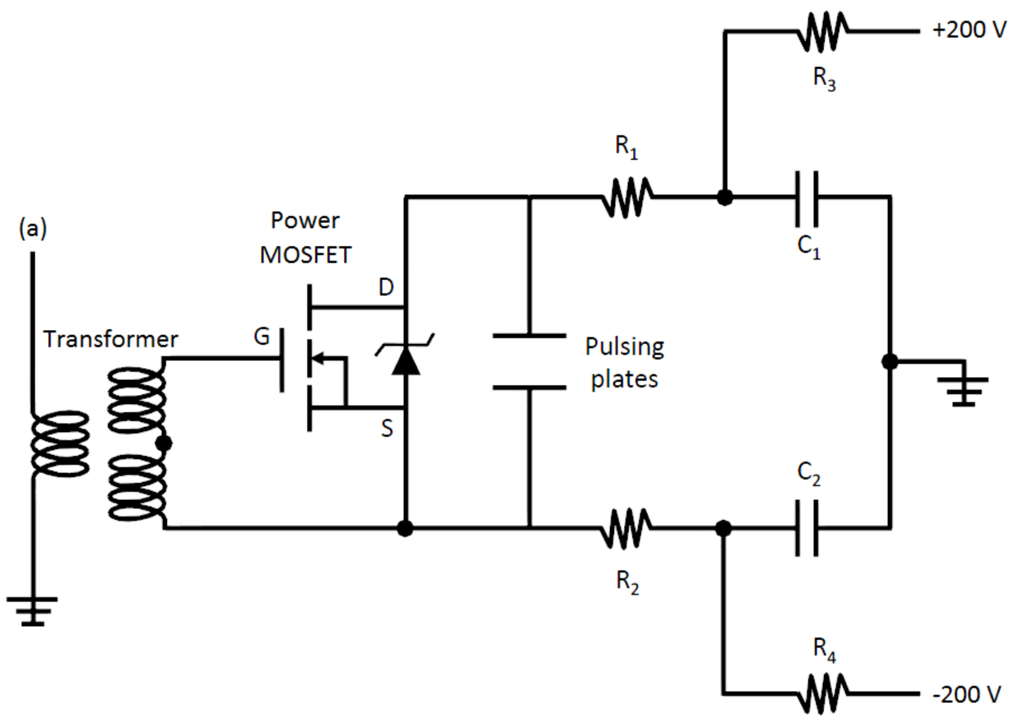

FIGURE 3.4. Pulsing circuit. $R_1 = R_2 = 470\ \Omega$, $R_3 = R_4 = 20\ \mathrm{k}\Omega$, $C_1 = C_2 = 680$ nF. [21]

$$I = \frac{-(V_{out} + R_1 C \frac{dV_{out}}{dt})}{R_1 M}. \tag{5}$$

R_1C and R_1M are determined for each pre-amp. The time constant R_1C is determined by fitting an exponential to the decay of a signal, and R_1M is a constant which is then determined by fitting this shaped signal to a known input square pulse. Final shaped currents for signals from the induction plates and cup 3 are shown in Fig. 3.5(right).

Pulsing data also provides confirmation that the beam is composed of Ba^+. The time between the center of the pulsing plate voltage overlap and the center of the pulse measured by the Faraday cup, along with a measurement of the distance traveled, provides a velocity measurement of the ions. This distance was measured to be 31.5 ± 0.5 cm, and time-of-flight

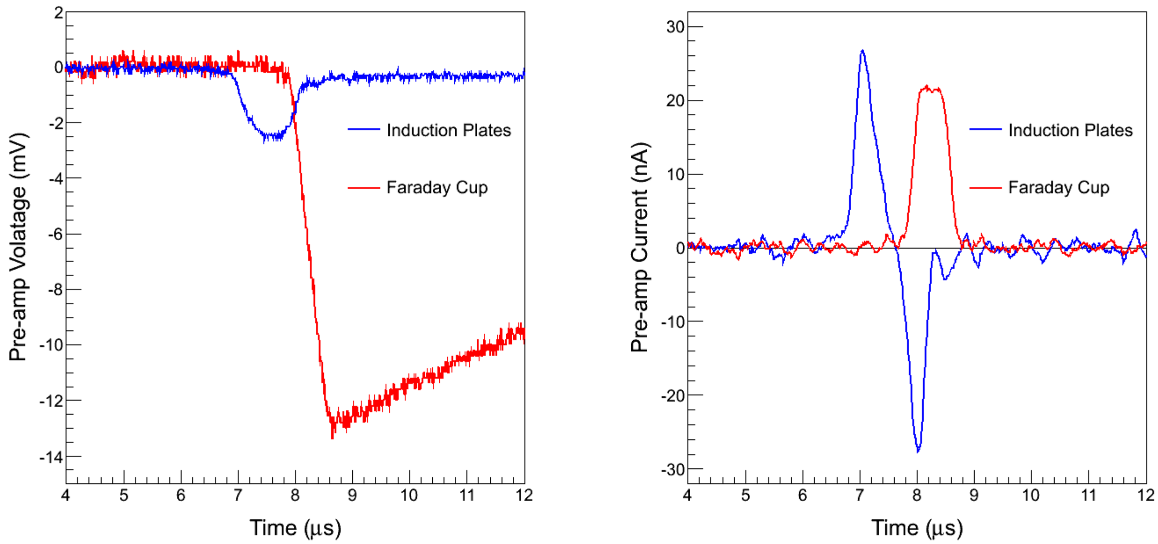

FIGURE 3.5. Raw (left) and shaped (right) pulse signals from induction plates and cup 3. The raw induction signal appears small because it is a less sensitive pre-amp (accounted for in shaping).

data, e.g. Fig. 3.6, give 39.8 ± 3.4 amu for Ar^+ and 136.8 ± 6.3 amu for Ba^+, including an uncertainty on the time of flight of ± 0.1 μs. This rules out any BaO^+ contribution to the Ba^+ ion beam.

3.1.5. CALIBRATION OF ION DEPOSIT. To calibrate the signal at cup 3 to an ion density at the sapphire window, another Faraday cup (cup w) is attached to the cold finger in place of the sapphire window. Firstly, the ratio in $\frac{fC}{pulse}$ between cup 3 and cup w is measured ($\equiv f$). Then, knowing the radius of cup w lets one determine the ion density per pulse at the sapphire window:

$$\frac{ions}{pulse \times m^2} = \frac{Cf}{Ae} \tag{6}$$

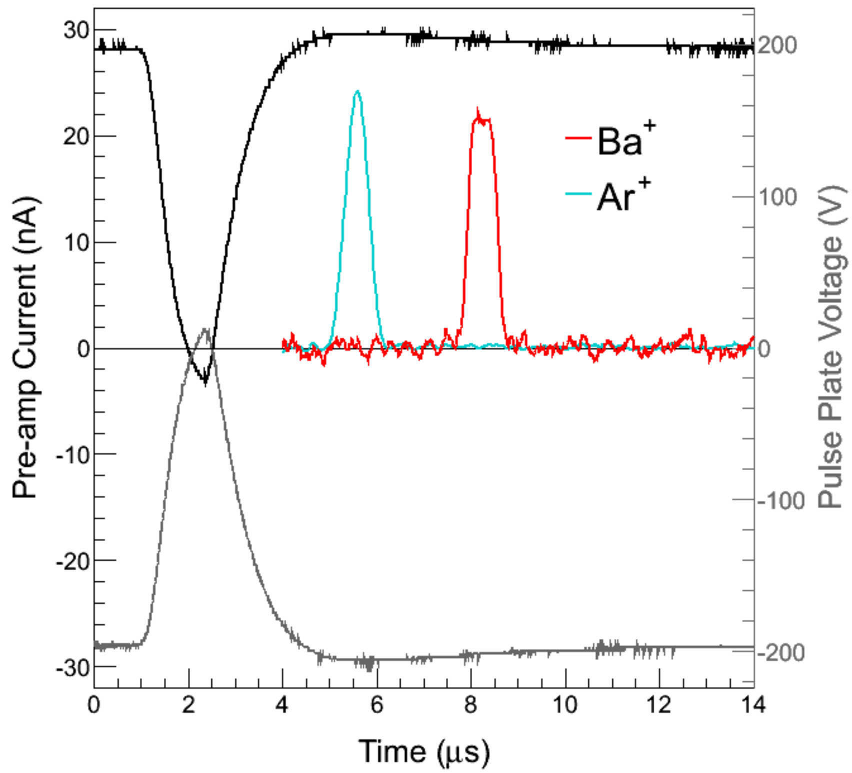

FIGURE 3.6. Arrival time of pulses at cup 3 vs. time of pulsing plate signal (black (+) and gray (-)) for Ar^+ and Ba^+.

where C is $\frac{fC}{pulse}$ at cup 3, A is the area of cup w, and e is the elementary charge. The required settings of the final deflection plates H2 and V2 are also determined by cup w. These typically differ from the peak values for cup 3 by about 70 V in H2 and 60 V in V2, corresponding to about 4 mm in x and y position at cup w.

3.2. Ba Getter Source

A $BaAl_4$ getter is employed as a purely neutral Ba source which can be inserted on a bellows to emit toward the sapphire window, shown in Fig. 3.7. Getters were used extensively in previous work [22] for measuring the absorption of Ba in SXe with large Ba deposits, and in identifying emission peaks. A getter is used briefly in this work in identifying the 619-nm fluorescence peak, as described in Chapter 4. Getters used in [22] were exothermic $BaAl_4$-Ni

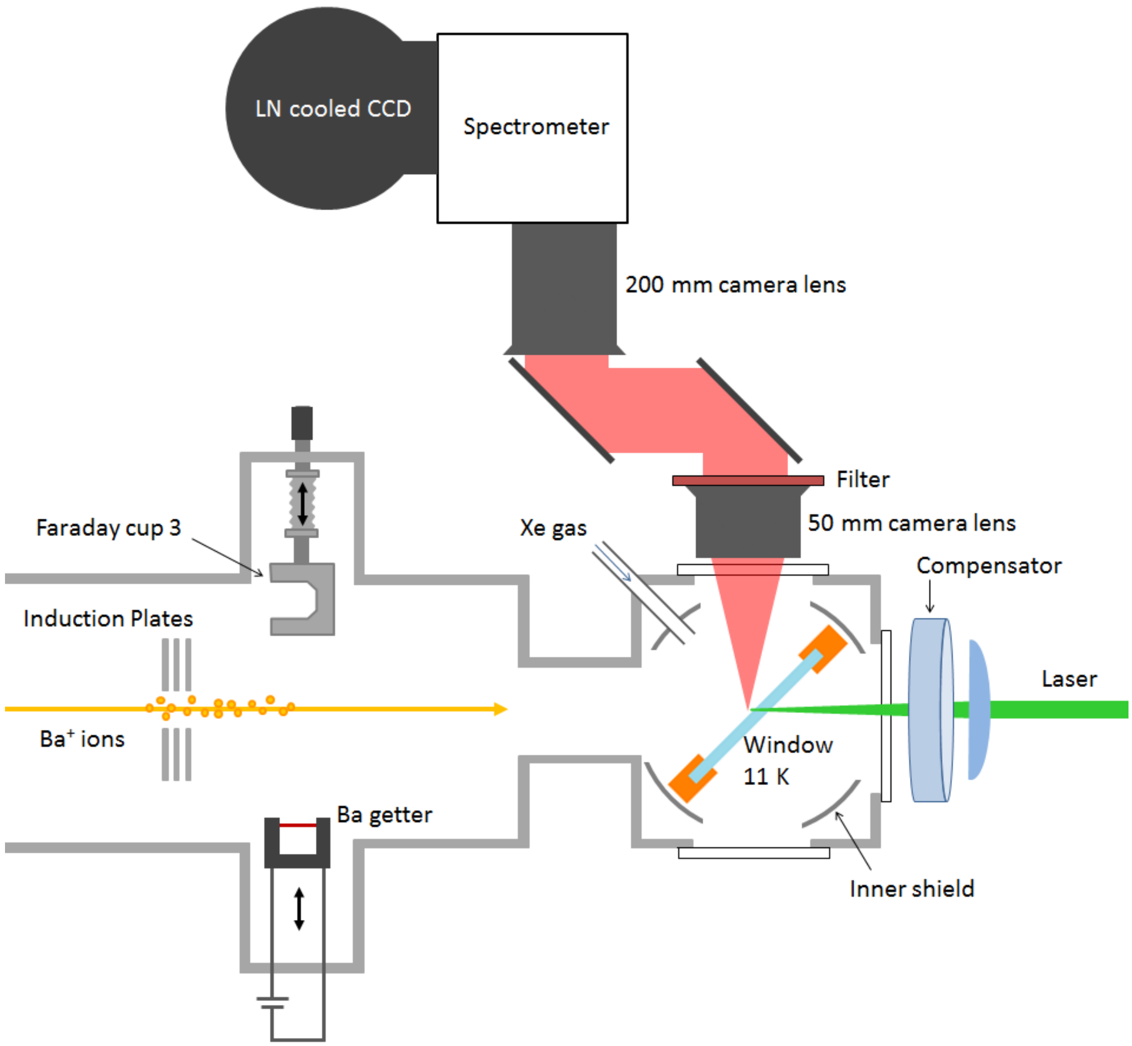

FIGURE 3.7. Apparatus around sapphire window, including Ba getter, and optics for excitation and collection.

flash getters. The getter used here is an endothermic type, designed for more controlled Ba emission.

3.3. Sample Deposition

The Ba^+/Ba is co-deposited with ultra-pure Xe gas onto a cold sapphire window. Sapphire has good thermal conductivity at low temperature and good optical transparency in the visible. The window is held to a coldfinger and is tilted at 45° to allow access of the ion beam as well as the excitation laser and collection optics. To begin a deposit, Xe gas

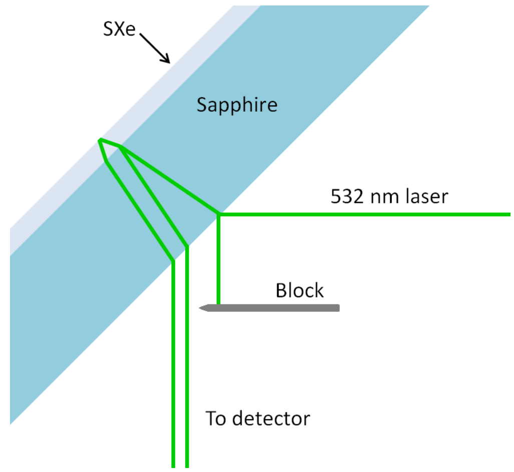

FIGURE 3.8. Setup for measuring SXe growth rate by interference fringes.

is flowed toward the window via a leak valve. Cup 3 is then retracted to clear the path for Ba^+ ions, which land in the SXe matrix as it grows. Cup 3 is then replaced, and the Xe leak stopped.

SXe matrix growth rate can be measured by interference fringes in a laser reflected against the front surface of the sapphire window, as shown in Fig. 3.8. Fringes for SXe deposition at 52 K and 11 K are shown in Fig. 3.9 for the leak rate used in this work. The refractive index of SXe has a negligible dependence on temperature between 50 and 30 K [23], so these can be compared directly. A somewhat lower rate is observed at 52 K, at 31 nm/s, vs. 37 nm/s at 11 K. To evaporate a sample, the window is heated to around 100 K, and fringes also appear during this process as well. The full set of fringes for a deposit at 52 K and its evaporation when heated is shown in Fig. 3.10, along with the window temperature. This shows that the SXe evaporates between 73 K and 78 K. Notice that the same number of fringes appear in the deposit and the evaporation.

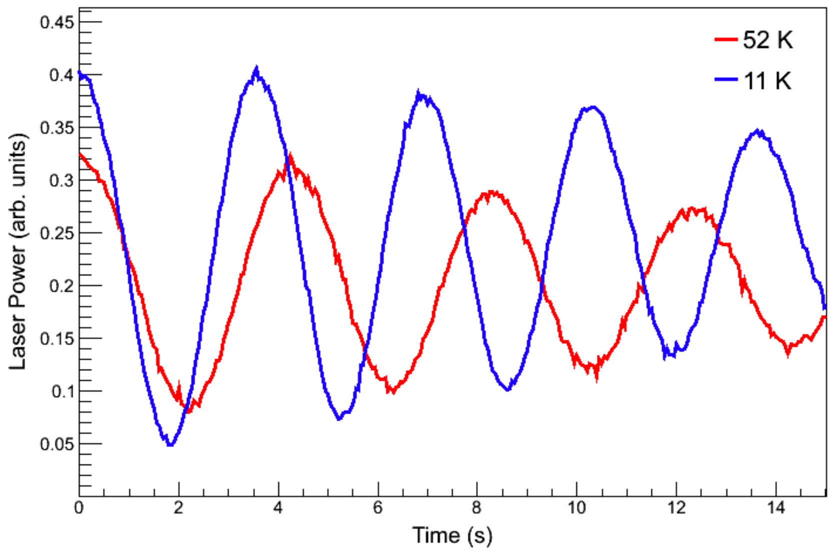

FIGURE 3.9. Interference fringes for the same Xe gas leak rate deposited on the sapphire window at 11 K and at 52 K.

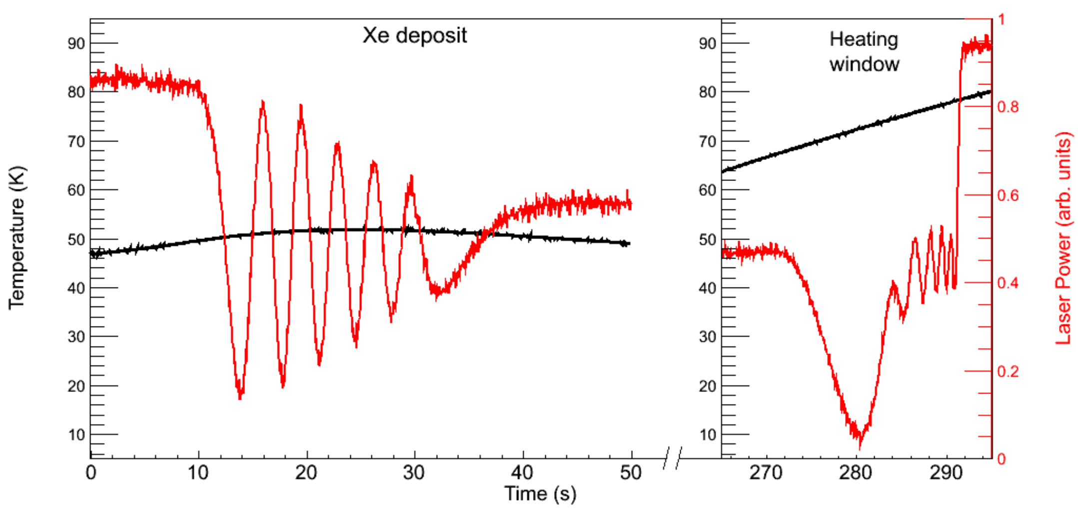

FIGURE 3.10. Interference fringes of a deposit at 52 K and of its subsequent evaporation when heating the sapphire window.

3.4. Laser Excitation

Green/yellow laser excitation is done with a Coherent 599 dye laser, pumped by the 514-nm line of a Lexel 3500 Ar ion laser. Rhodamine 110 (R110) dye tunes over 542 - 566 nm, and Rhodamine 6G (R6G) tunes over 567 - 590 nm. Another Coherent 599 contains Coumarin 480 dye for blue excitation, which is pumped by a Kr ion laser.

An aspherical lens focuses the laser into the cryostat from the side (Fig. 3.7). This lens reduces spherical aberration in the laser focus so that it can reach the diffraction limit. However, to reach the diffraction limit in the SXe, astigmatism introduced by the tilted sapphire window must be corrected. To do this, compensating astigmatism is introduced by 1-cm thick fused silica optical flat, placed after the lens, tilted in the y-plane whereas the sapphire window is tilted in the x-plane. The proper angle for the compensator is determined by a ray matrix equation, Eq. x:

Where ... f(w?) is measured ... The effect of the SXe layer is negligible since its thickness if less than a wavelength.

show measurements of astig. w/ and w/o compensator. Astigmatism in the laser itself was measured to be consistent with zero.

3.5. Collection Optics

Fluorescence is collected above the cryostat (Fig. 3.7). A 50 mm Nikon camera lens collimates the light, and a fluorescence filter sits on top of it. A band-pass filter is used for imaging, and a Raman filter is used for spectroscopy. The fluorescence then reflects off two steering mirrors, and is imaged by a 200 mm Nikon camera lens on a Roper Scientific liquid-nitrogen-cooled CCD, where it is imaged with a magnification of 4.

The CCD has a removable Princeton Instruments imaging spectrometer. In this case, the 200 mm camera lens focuses the light onto an inlet slit, which is then imaged by the spectrometer onto the CCD after reflecting off a diffraction grating. The 0-order reflection of the grating provides an image for alignment, and it can be tilted to distribute the 1^{st}-order reflection across the horizontal CCD pixels for doing spectroscopy. When a 1" diameter filter is used, the system has a collection efficiency (ϵ_c) of about 1.5% without the spectrometer, and about half of that with the spectrometer due to a grating efficiency of 50%. The spectrometer will also limit the system to an f-number of 4.

To limit laser exposure to only the time of CCD exposure, a laser shutter is linked to the camera exposure with a LabVIEW program. This program also records laser power via a calibrated pickoff, as well as the temperature of the coldfinger near the sapphire window during observation.

3.6. Laser Scanning

In order to obtain images of separated single atoms, the laser focusing lens is attached to motorized Newport translation stages which scan the laser position by scanning the lens in x and y, shown in Fig. 3.11. These stages are in addition to a manual z translation stage for laser focusing. An extension of the aforementioned LabVIEW program coordinates movement of these stages such that x or y position is stepped in between CCD frames, and each frame then corresponds to a position in a laser scan grid.

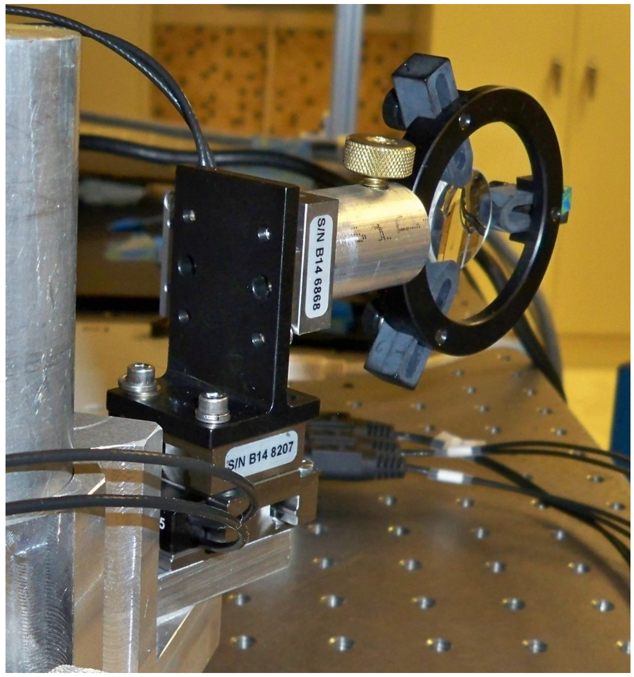

FIGURE 3.11. *Put pic of new ones? Otherwise w/ asphere at least.*

CHAPTER 4

Results

Improved studies of several emission peaks of neutral Ba in SXe, which are first reported in the theses of B. Mong [ref] and S. Cook [ref], are reported. The bleaching of several of these peaks is carefully observed (do a correction on p-meter sensitive area and on p-meter quantum efficiency, and also a spherical aberation correction for power??), and a model of atomic transition rates is fit to this data. Improved excitation spectra are achieved for all observed Ba emission peaks. Images of $\leq 10^{3?}$ Ba atoms are achieved using the bleaching peaks. Ultimately, images of Ba atoms at the few-atom level are achieved using the 619-nm fluorescence peak. Improved studies of candidate fluorescence peaks of Ba^+ in SXe are also reported. *Where/how should I reference the ba spec paper?*

4.1. Fluorescence of Ba in SXe

The multiple peaks observed from deposits of Ba in SXe are attributed to Ba atoms occupying different Xe matrix sites, the phenomena of which are described in Chapter 3 (*ref chap theory doesn't work*). Fig. [ref fig spectra for 10K, 50K, annealed 10K] shows spectra of Ba deposits under different conditions. A deposit made at 11 K shows a different ... um how is this described in the paper?

excitspec of 50 K [fig of all, including r110 of 619]... and 10 K?

leak rate dependence?

4.1.1. Identifying Peaks as Ba in SXe.

This section was claimed in Ba getter section of Chapter 3 to talk about getter use in identifying 619.

4.2. Bleaching

590 etc, model fit (see results intro paragraph)

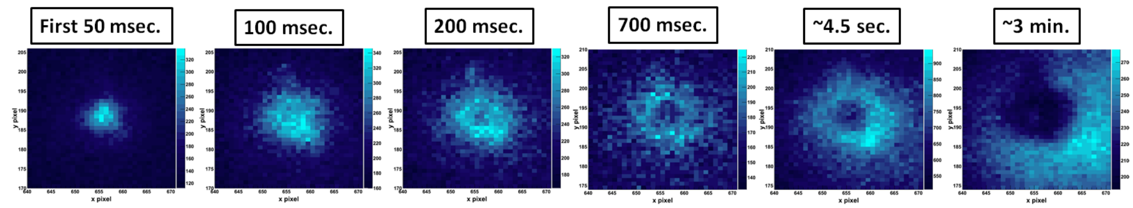

Figure 4.1

619, with the changes in time and I

4.3. Imaging

4.3.1. Imaging 577- and 591-nm peaks.

4.3.2. Imaging 619-nm peak.

CHAPTER 5

Conclusions

5.1. Future Steps

Talk about whatever Chris will do next ... ions? Other sites? Populations?

Talk about Adam's work, show pics and stuff.

Bibliography

[1] C.D. Ellis and W.A. Wooster, “The average energy of disintegration of radium e,” *Proceedings of the Royal Society (London)* **A117** 109-123 (1927).

[2] F. Wilson, *American Journal of Physics* **36**, 12 (1968).

[3] Y. Fukuda *et al.* (Super-Kamiokande Collaboration), *Phys. Rev. Lett.* **81** 1562 (1998).

[4] S.T. Petcov, W. Rodejohann, T. Shindou, Y. Takanishi, *Nuclear Physics B* **739**, 208233 (2006).

[5] M. Danilov *et al.*, *Physics Letters B* **480**, 1218 (2000).

[6] K.A. Olive *et al.* (Particle Data Group), “14. Neutrino Mass, Mixing, and Oscillations,” *Chin. Phys. C* **38**, 090001 (2014) (http://pdg.lbl.gov)

[7] P.A.R. Ade *et al.* (Planck Collaboration), *Astronomy and Astrophys.* **571**, A16 (2014).

[8] N. Steinbrink *et al.*, *New Journal of Physics* **15**, 113020 (2013).

[9] J. Albert *et al.* (EXO-200 Collaboration), *Phys. Rev. C* **89**, 015502 (2014).

[10] M. Moe, *Phys. Rev. C* **44**, R931 (1991).

[11] M. Auger *et al.*, *JINST* **7**, P05010 (2012).

[12] R. Nielson *et al.*, *Nuclear Intruments and Methods in Physics Research A* **608**, 68 (2009).

[13] E. Conti *et al.*, *Phys. Rev. B* **68**, 054201 (2003).

[14] J. Albert *et al.* (EXO-200 Collaboration), *Nature* **510**, 229 (2014).

[15] N. Ackerman *et al.* (EXO-200 Collaboration), *Phys. Rev. Lett.* **107**, 212501 (2011).

[16] A. Gando *et al.* (KamLAND-Zen Collaboration), *Phys. Rev. C* **86**, 021601 (2012).

[17] K. Twelker *et al.*, *Review of Scientific Instruments* **85**, 095114 (2014).

[18] B. Mong *et al.*, *Phys. Rev. A* **91**, 022505 (1954).

[19] T. Brunner et al., *International Journal of Mass Spectrometry* **379** (2015) 110-120.

[20] L. Wåhlin, "The Colutron, a Zero Deflection Isotope Separator," *Nuclear Instruments and Methods* **27** 55-60 (1964).

[21] S. Cook, *Detection of Small Numbers of Barium Ions Implanted in Solid Xenon for the EXO Experiment.* Colorado State Universtiy Thesis/Dissertation (2012).

[22] B. Mong, *Barium Tagging in Solid Xenon for the EXO Experiment.* Colorado State Universtiy Thesis/Dissertation (2011).

[23] A. C. Sinnock, *J. Phys. C: Solid St. Phys.* **13**, 2375-91 (1980).